Hydrogel Assisted Double Molding of 3D-Print Enables Prestress Regulation of Micro-Heart Muscle Physiology

Daniel W. Simmons[1], David R. Schuftan[1], Jingxuan Guo[2], Kasoorelope Oguntuyo[1], Ghiska Ramahdita[2], Mary K. Munsell[1], Brennan Kandalaft[1], Missy Pear[1], Nathaniel Huebsch[1,#]

Author affiliations:

[1]Department of Biomedical Engineering, Washington University in St. Louis McKelvey School of Engineering, St. Louis, MO 63130

[2]Department of Mechanical Engineering & Materials Science, Washington University in St. Louis McKelvey School of Engineering, St. Louis, MO 63130

[#]Corresponding author:

Nathaniel Huebsch, PhD, Assistant Professor of Biomedical Engineering

One Brookings Drive

Whitaker Hall, Room 290D

Saint Louis, Missouri, 63130, United States.

Phone: 314-935-3534

Email: nhuebsch@wustl.edu

Abstract

Tissue engineered *in-vitro* models are an essential tool in biomedical research. Tissue geometry is a key determinant of function, but controlling geometry of micro-scale tissues remains a challenge. We developed a new double molding approach that allows precise replication of high-resolution stereolithographic prints into poly(dimethylsiloxane), facilitating rapid design iterations and highly parallelized sample production. Hydrogels are used as an intermediary mold, and gel mechanical properties including crosslink density predict replication fidelity. We leveraged this approach to study the effects of geometry on the electrophysiology of miniaturized heart muscles engineered from human induced pluripotent stem cells (iPSC). Geometries predicted to increase tissue prestress globally affected cardiomyocyte structure and tissue electrophysiology. Strikingly, pharmacologic studies revealed a prestress threshold is required for sodium channel function. Analysis of RNA and protein levels suggest electrophysiology changes were related to post-transcriptional and potentially post-translational changes of the gap-junction protein Connexin 43 and the sodium channel Nav1.5.

Main

Human induced pluripotent stem cell-derived cardiomyocytes (iPSC-CM) are promising alternatives to current *in-vitro* methods (e.g., hERG assays) for predicting drug-induced arrhythmias [1]. However, iPSC-CM are immature compared to adult cardiomyocytes, diminishing their utility as a model system [2]. Tissue engineering approaches have been applied to enhance iPSC-CM maturity and thereby more accurately predict pro- and anti-arrhythmic drug effects [3], [4], [5], [6] [7]. Increased prestress on cardiomyocytes cultured in aligned 3D engineered tissue environments has been hypothesized as a key physical cue to induce maturation [8], analogous to how forces like prestress regulate *in-vivo* heart formation and function [9], [10], [11].

To test the impact of prestress in 3D tissues on electrophysiology maturation, we sought to create micro heart muscle arrays (µHM) of various geometries, as simple continuum mechanics models of tissue compaction predict a direct link between tissue geometry and prestress [8]. Soft lithography is a common technique for creating molds to control the geometry of micro-scale engineered tissues, but is time consuming, requires specialized facilities, and limits the complexity of devices produced [12], [13]. Due to these inherent limitations, we turned to high resolution 3D-printing for mold creation. High resolution stereolithographic (SLA)

3D-printing has been suggested as a replacement for soft lithography to enable rapid fabrication of micro-devices [14]. However, photo-crosslinked materials used for SLA printing inhibit crosslinking of elastomers like poly(dimethylsiloxane) (PDMS) which remain the most frequently used material for micro-devices (Fig. 1A) [15], [16], [17], [18], [19], [20]. Various methods have been attempted to directly mold PDMS off 3D-prints [15], [16], [17], [21], [18], [20]. However, these approaches are highly user dependent and inconsistent [15], [16].

As SLA printing involves free-radical crosslinking, we hypothesized SLA prints act as a sink of the free-radicals necessary for PDMS curing (Fig. 1B). To enable consistent PDMS replication of high-resolution 3D-prints, we developed a double molding technique inspired by lost wax casting [22], where a second, intermediary material is used to transfer features from 3D-prints into PDMS. A similar approach has been described with epoxy [23], but this brittle material is incompatible with molding complex shapes that are damaged upon intermediary removal from the print [20]. Surprisingly, this approach has not been reported with hydrogels intermediaries, despite the wide variety of gels that exhibit free-radical independent crosslinking and have mechanical properties tailorable over a wide range [24]. We found that given optimal post-crosslinking mechanical properties, free-radical independent hydrogels are ideal intermediaries to replicate high-resolution SLA prints into elastomers, such as PDMS (Fig. 1C).

To test the potential of Hydrogel Assisted STereolithographic Elastomer prototyping (HASTE), we attempted replica molding of dogbone-shaped features off SLA prints using two types of gels, agar and alginate. Both polymers crosslink independently of free radicals, through either physical chain entanglement (agar), or a combination of covalent (carbodiimide) and ionic (calcium) crosslinks (alginate). Both hydrogels were broadly capable of enabling PDMS crosslinking (Fig. 1D), with post-crosslinked mechanical properties predicting replica molding success (Fig. 1E-F, Fig. S1). Hydrogel crosslink density predicted replication success, alongside compressive toughness and ultimate modulus, which most strongly correlated to replication fidelity. These data suggest that the ability of the hydrogel to be removed from the 3D-print without plastic deformation (toughness and ultimate modulus), alongside limited hydrogel water loss during PDMS crosslinking (crosslink density), are the most important considerations for this application.

Using optimized hydrogel formulations (1.5% agar and 1% high molecular-weight (HMW)/2% low molecular-weight (LMW) alginate), we next demonstrated the ability of HASTE to replicate 3D-printed features that are difficult or impossible to create using standard soft lithography, including a geodesic dome (Fig. 1G) and micro-TUGs (T-shaped pillars, an alternative mold for engineering heart tissues (Fig. 1H) [25]). Scanning electron micrographs of these features highlights the high resolution of HASTE. In addition to the 1:1 reproduction of the 3D-print into PDMS, the ~15µm z-axis resolution of the 3D-printer used is reproduced in the final PDMS replicate (Fig. 1G). Although 0.75% agar can replicate the major features of the geodesic dome, increasing concentration further increased replication fidelity of fine features, as seen in replication of the original 3D-print's z-axis resolution (Fig. S1B). 1.5% agar and 1% HMW/2% LMW alginate replicated features with similar fidelity, although alginate maintained a smoother surface (Fig. S1C). Although high concentration agar (>1.5% wt/v) achieved higher replication scores when molding dogbone-shaped extrusions, we found these concentrations also increased viscosity and gelation speed, often leading to air bubble formation and decreased replication efficiency (data not shown). For simple 2D extrusions up to ~2mm in height, 1.5% w/v agar provided adequate replication. For more complex 3D features or those with larger height, the tougher 1% HMW/2% LMW alginate was better suited. For example, when replicating frames with a wall thickness and height of several mm, the agar tore when attempting to remove the relatively thin gel off the print (Fig. S1D).

We next used HASTE to create dogbone-shaped molds, with a progressively lengthened "shaft" connecting "knobs" on either end, to test whether prestress directly affects morphology of iPSC-CM utilized after 15 days of differentiation [26] (Fig. 2A). µHM designs were hypothesized to increase tissue prestress as shaft length increased based on COMSOL modeling (Fig. 2B), and previous literature demonstrating tissue geometry passively affects cell alignment and tissue prestress [8], [27]. Brightfield imaging of tissues (µHM day 15, µD15) revealed gross tissue morphology was largely unaffected by tissue shaft length, although 2mm tissue had slightly more lateral compaction (Fig. 2C-D). Despite the subtle changes in overall tissue shape, tissue geometry had marked effects on cardiomyocyte structure (Fig. 2E-H). Nuclear alignment, aspect ratio, and overall cellular length all increased as shaft length increased from 0mm (3D tissue with no axis alignment)

to 2mm (Fig. 2E-F). Interestingly, although cell length increased with shaft length, cell width was unchanged (Fig. 2G-H), suggesting eccentric hypertrophy [11]. Consistent with model predictions, changes to nuclear and cell morphology were most pronounced in the tissue shaft and not the knobs (Fig. S2). Collectively, these results confirm that geometry controls compacted tissue prestress and cellular morphology.

We next investigated potential effects of prestress on electrophysiology of spontaneously beating µHM. Both action potential and calcium transient waveforms were strongly affected. Broadly, the action potential upstroke duration increased with tissue length, as well as the action potential duration and calcium transient decay (Fig. 3A). Analysis of several key action potential (time to 90% duration, APD_{90}) and calcium transient (decay time from peak to 25% above baseline, τ_{75}) parameters quantitatively captured these prestress-induced global changes (Fig. 3B, S3B). Importantly, analysis of individual electrophysiological parameters suggested no measurable changes in timing whether the entire tissue or a sub-region was analyzed (Fig. S3A). This suggests that µHM electrophysiological behavior is dominated by the tissue's highest-prestress regions.

Consistent with more mature, ventricular-like phenotypes [28], µHM with longer shafts exhibited slower rates of spontaneous beating (Fig. 3C). Interestingly, beat-rate corrected action potential upstroke duration (cUPD) increased with prestress. APD_{90} also followed this trend and increased alongside tissue prestress (Fig. 3C, S3C, S3D). Increases in time required for the action potential and calcium transient upstroke may be reflective of *decreased* sodium current, which would suggest less mature tissues, or may instead reflect *increased* gap-junction coupling of cells, which slow action potential and calcium upstroke timing in tissues [29]. To address this question, we analyzed the spontaneous conduction speed across µHM, and found no significant difference between µHM with 1 vs 2mm shaft lengths at any time point, although the conduction speed increased over time in all geometries (Fig. 3D).

We next assessed the effects of a specific sodium current (I_{Na}) inhibitor, saxitoxin. 3D tissues with no preferential alignment (0mm) showed no significant cUPD changes in response to saxitoxin across a broad dose range, suggesting that I_{Na} is non-functional in such tissues (Fig. 3E). Strikingly, aligned tissues (µHM with

either 1 or 2mm shaft length) exhibited an appropriate dose-response with increasing cUPD as I_{Na} block increased (Fig. 3E). These observations suggest a prestress threshold is necessary for proper contribution of the Nav1.5 ion channel to the action potential. Although the 1 & 2mm tissues show similar I_{Na} blockage curves in relation to cUPD, the 2mm tissue consistently maintain a higher cUPD. This increased cUPD could be due to increased Nav1.5 expression, leading to a greater influx of Na^+, and thus Ca^{2+}, into the cells. Altogether, these observations alongside conduction measurements (Fig. 3D) suggest the increased upstroke time in µHM with anisotropic, elongated geometry is more likely to reflect increased gap-junction coupling rather than Nav1.5 deficiency. In contrast to observations with I_{Na}, blockade of either the *L*-type calcium current (I_{CaL}) with Nifedepine or the rapidly rectifying potassium current (I_{Kr}) with E4031 revealed no marked prestress-dependent changes in these currents (Fig. 3F,G, S4B,C). Because µHM showed similar calcium UPD during I_{CaL} blockage, it is likely that calcium transient differences seen (Fig. 3A) are unrelated to calcium release mechanisms (I_{CaL} or calcium-induced calcium release from the sarcoplasmic reticulum). Instead, they may be due to differences in I_{Na} that allow more calcium to enter the cell. Likewise, increases in APD_{90} with tissue prestress are unlikely to be caused by changes in I_{Kr} (Fig 3G).

To determine potential molecular mechanisms causing differential I_{Na} in µHM, we first quantified RNA expression for a variety of mechanical proteins and action potential related ion channels (Fig. 4A). Although we observed significant upregulation of several transcripts encoding structural proteins when comparing µHM to the input iPSC-CM (Fig. S5), transcriptional changes were unchanged as a function of µHM geometry (Fig. 4A). This is consistent with previous work reporting an apparent decoupling between transcript levels and function of individual ion channels [30]. Quantification of cardiomyocyte entry into proliferative stages of the cell cycle via Ki67 staining also did not indicate an effect of µHM geometry (Fig. S6). Together, these data suggest that prestress induced changes observed in electrophysiology do not require global maturation.

We next assessed the expression and localization of key membrane-localized proteins in µHM. Plakophilin-2, a major component of the desmosome associated with function of both of these proteins [31], was localized correctly to cell-cell junctions regardless of tissue prestress (Fig. 4B). In contrast, we observed a

trend toward increased Nav1.5 and Connexin-43 (Cx43) expression in the shaft region of elongated tissues, without any indication of mis-localization in 3D tissues with no preferential axis of alignment (Fig. 4B). Analyzing bulk protein levels over entire μHM, indicated a trend toward increased Cx43 protein expression in elongated μHM (1 and 2mm shafts), similar to other studies [5] (Fig. 4C). However, this trend was not statistically significant (p = 0.099, 2-way t-test) over 5 batches of μHM, and analysis of overall $Na_V1.5$ protein levels revealed no similar trend. These observations suggest that robust protein expression differences require longer culture time in the μHM environment. Given a half-life of 1-3 hours [32], and a disconnect between gene and protein expression [30] in Cx43, it is likely that changes we observe in μHM upstroke duration (Fig. 3B) are related to post-translational changes in Cx43. Trafficking may be a key post-translational change in Cx43 and Nav1.5 in μHM. Cx43 and Nav1.5 trafficking are dependent on prestress sensitive structures (microtubules and focal adhesions [33], [32], [34], [35],[36]). These trafficking changes may be sufficient to drive marked functional changes in I_{Na} without requiring gross changes in the overall levels of the transcript or protein encoding for the functional pore-forming subunit of the sodium channel.

Overall, our results reveal the importance of tissue prestress on electrophysiological function of cardiomyocytes. Importantly, prestress alone is sufficient to drive a lower spontaneous beat-rate and functional $Na_V1.5$ current after only two weeks of culture. However, no level of prestress was able to eliminate spontaneous beating at this timepoint, and action potential upstroke is still highly Ca^{2+} dependent. These observations suggest that combining geometric constraints with chemical stimuli may be required to induce further electrophysiological maturation [28]. The HASTE method developed here enables facile, iterative changes in the geometric boundary conditions used to form engineered tissues and organoids to determine how the distribution of stresses within these systems affects cellular identity and physiology.

Methods

Formation of 3D-Prints

Using Solidworks, the stencil mold was created by first extruding a rectangular base several millimeters thick to prevent warping during the polymer crosslinking process, and eventual print removal from the printer. On top of this base an individual dogbone shape is designed and extruded to a height of 1 mm. Using linear patterning we can easily create groups of dogbones, typically clustered in groups of 3 with several millimeters of spacing between groups. This allows us to easily cut and place groups into wells of a 24 well plate. The individual dogbone shapes have a 1 mm x 1 mm knob/square on each end, with a 400 µm wide shaft of variable length. Importantly, dogbones within a cluster should be spaced at least 2 mm apart from one another to prevent a syncytium of tissue from “bridging” between adjacent micro-muscles (Fig. S7).

HASTE Double Molding Process

We have created a double-molding method to enable replication of 3D-printed molds into PDMS. A negative of the 3D-printed mold is first created by casting off a hydrogel (Fig. 1 A-C). Sylgard 184 (Dow Corning) is mixed according to the manufacturer’s instructions, poured onto the hydrogel negative, degassed, and cured at 37°C for 8+ hours to form a PDMS positive of the 3D-printed mold. We have utilized both agar and alginate hydrogels for the double molding process. Both hydrogels were found to be broadly capable of enabling PDMS replication of 3D-printed stereolithographic features because they did not inhibit PDMS crosslinking.

Agar (Fisher BP9744-600, lot # 193828) was tested at 0.25% to 3% w/v. Gels were formed by dissolving agar in boiling tap water, then allowed to cool to <60° C before pouring onto the 3D-print. It is then chilled in a 4° C refrigerator for 20+ minutes before removal.

Two alginates were tested, which we designated as high (HMW) (FMC Manugel GMB Lot# GB0406101) and low molecular weight (LMW) (Dupont Manugel GHB Lot# GD0708801). These two alginates were dissolved in 0.1 M 2-(N-morpholino)ethanesulfonic acid (MES) buffer (pH between 6 & 7), and were tested both individually and mixed at multiple ratios. They were crosslinked to form double-network hydrogels, containing both ionic and covalent crosslinks. Covalent crosslinks were formed using adipic-acid-dihydrazide/1-ethyl-3-(3-dimethylaminopropyl)-carbodiimide as previously described [37]. To enable slow-forming ionic

bonds, calcium chloride was bound to EDTA and dissolved in 0.1M MES at pH ~7.2. Glucono-delta lactone was dissolved into the gels to slowly release the chelated calcium via pH acidification. However, low pH alginate gels were found to inhibit PDMS crosslinking, so the fully-crosslinked alginate negatives of the 3D-prints were soaked in 0.1 M MES containing 25 mM CaCl2 with a pH between 8-9 for 12+ hours, then removed and placed in a 37°C oven for 1.5-2 hours to de-humidify. The incubator contained 3+ liters of water within a large jug to help maintain humidity. PDMS (Sylgard 184) was then mixed, poured over the hydrogel negative, degassed, and allowed to crosslink overnight in the 37°C incubator containing the water jug to create the final stencil mold.

Hydrogel Characterization

Compressive mechanical testing of gels was conducted on a TA Instruments ElectroForce 3200, using the 225 N load cell. Gels were pre-compressed to 0.1N, after which compression testing was conducted at 1mm/min to gel failure. The Electroforce was located in Washington University's Department of Mechanical Engineering & Material's Science Shared Instrument Group.

Gel weight was measured both immediately after crosslinking and after the gel was allowed to dry completely. Swelling ratio was measured as: (crosslinked gel weight – dry gel weight) divided by the dry gel weight. The hydrogel crosslink concentration was calculated as previously described [38]. The polymer density of alginate [39] and agar [40] have been previously reported.

Quantification of Feature Transfer Fidelity

To enable qualitative scoring of gel transfer fidelity, PDMS replications of dogbones were created for all gels tested. PDMS replicates were pressed into red stamp pads, depositing ink onto the surface of the prints to enable visualization of the top-most surface of the dogbone features (Fig. 1D). The PDMS replicates were imaged and given a score by a researcher based on their opinion of the feature transfer quality on a 1 to 5 scale, where 5 is a perfect replication and 1 is a complete failure to replicate the original 3D-printed dogbone. Example images are given to show visual differences between replication quality given by different gels and how they were qualitatively score (Fig. 1D).

To enable quantitative score, PDMS replicates were similarly created of dogbones and pressed into ink. Outlines of the topmost surface, covered in red ink, were manually drawn. These outlines were then compared to an outline of the original 3D-print, using the built-in Procrustes function in Matlab.

Scanning Electron Microscopy

PDMS replications of 3D-printed features were imaged using at Thermofisher Quattro S Environmental Scanning Electron Microscope under high vacuum using 1.0 kV with a 3.0 spot size, within Washington University's Institute of Materials Science & Engineering.

Stem Cell-Derived Cardiomyocyte Production

"Wild Type C" human induced pluripotent stem cells (iPSC) were created at the Gladstone Institutes of Cardiovascular Disease (Coriell Institute GM25256), and were modified via knock-in of a single copy of GCaMP6f into the AAVS1 "safe harbor locus" [28]. iPSC were cultured at 37°C in Essential 8 media on 6-well plates coated with growth factor-reduced Matrigel. Once approximately 85% confluency was reached, the cells were passaged into new wells using Accutase. iPSC were differentiated into cardiomyocytes using small molecule manipulation of Wnt signaling [26].

µHM Formation

The PDMS replicates of the 3D-printed molds were oxidized using air plasma (Harrick Plasma) for 90 seconds at high power. These were then treated with trichloro(1H,1H,2H,2H-perfluorooctyl)silane via vapor deposition to enable PDMS-off-PDMS molding for final stencil creation. Stencil molds with "dogbone" shaped through-holes were formed by pouring Sylgard 184 over the treated PDMS molds, clamped between glass/acrylic plates and cured at 60°C for 4+ hours. Each dogbone shaped through-hole is 1mm thick, and three different dogbone sizes were created: 1) a tissue that is just a 1 mm x 1 mm knob with no shaft ("0 mm"), 2) a tissue with 1 mm x 1 mm knobs and a 400 µm x 1 mm shaft ("1 mm"), and 3) 1 mm x 1 mm knobs and a 400 µm x 2 mm shaft ("2 mm") (Fig. 1B).

Here we utilized stencils of varying shaft length (0, 1, & 2mm long), hypothesized to modulate tissue prestress alongside increasing shaft length without the need to dynamically modulate tissue length. A Comsol model was used of a linear elastic material confined to the dogbone shape, adherent to the substrate only in the knob ends. With an initial strain of -0.5 for each axis (x,y, z), isotropic shrinkage of the µHM volume by

82.5% was performed, compared with initial 100% dogbone-like volume. This modeling revealed step-wise increases in tissue prestress within the center of the tissue shaft.

To seed the PDMS stencils, they were cut, dipped in methanol, and placed into the wells of tissue culture well plates. The well plate was then placed into a 60°C oven overnight to reversibly bond the PDMS stencil to the well surface. The well was then coated with fibronectin to enable cardiomyocyte attachment to the substrate.

Un-purified iPSC-CM were singularized using 0.25% trypsin and seeded at a density of 7.5*10^7 cells/mL at 3 µL per individual µHM (~225,000 cells per tissue) without exogenous matrix. Seeded cells were incubated at 37°C for 30-60 minutes before adding media to limit cell loss, using DMEM with 20% FBS, 10 µM Y-27632, 150 µg/mL L-ascorbic acid, 4 µg/mL Vitamin B12, and 3.2 µg/mL penicillin. µHM typically began spontaneous beating within 24-48 hours of seeding; upon observing beating tissues the media was changed to RPMI/B-27, 150 µg/mL L-ascorbic acid, 4 µg/mL Vitamin B12, and 3.2 µg/mL penicillin (collectively called R+ media). µHM were then fed R+ media every 2-3 days until termination.

Immunohistochemistry

Tissues were fixed using increasing concentrations of paraformaldehyde from 1% to 4% [6], [7]. PDMS stencils were then removed, and tissues were embedded in 1% agar dissolved in MilliQ water. The agar-embedded tissues were then cryoprotected using 15% and 30% sucrose, flash frozen in OCT and cryosectioned at 8-15 um. Sectioning was done parallel to the tissue longitudinal axis. Samples were permeabilized with 0.1% Triton-X-100 for 20 minutes and blocked using 5% BSA in 0.1% Triton-X-100 for 45 minutes at room temperature. Primary antibodies were incubated overnight at 4°C, secondary antibodies were incubated at room temperature for 2 hours, and cell nuclei (Thermo Fisher Hoechst 33342) were stained at room temperature for 10 minutes. The samples were then protected against photobleaching with ProLong Gold (Invitrogen P36930), and imaged on an Olympus confocal microscope (Fluoview FV1200, Tokyo, Japan). Specific primary antibodies are listed in Table S2.

Cell Morphology Quantification

All images were quantified using ImageJ. Nuclear aspect ratio was quantified as the nuclear major axis length divided by the minor axis length, where a value of 1 indicates a perfectly spherical nucleus. Nuclear

alignment was quantified as the percentage of nuclei whose major axis aligned along the same vector, where a value of 1 indicates the major axis of all nuclei were perfectly parallel to each other. Cell length and width were quantified by staining the cell membranes with wheat germ agglutinin (ThermoFisher W849).

Resting sarcomere lengths were measured by staining for sarcomeric α-actinin. Images were analyzed by users blinded to the experimental conditions and tissue size. Within ImageJ users selected multiple representative regions within the tissue image. Within each region, the “straight line” function of Image J was used, after which “Plot Profile” was used to generate a 1D distance-intensity plot. The mean distance between peaks was then calculated to determine resting sarcomere length. A minimum of 10 regions for each tissue section tissue recorded; the data reported are mean values of these regions combined, with each data point representing an individual μHM.

Quantitative PCR

Total RNA was purified from tissues according to the manufacturer’s instructions using RNAqueous Total RNA Isolation Kit (Invitrogen AM1912). Additional steps were conducted to inactivate DNases. cDNA was then synthesized from the resulting RNA using oligo(dT)20 and SuperScript III (Invitrogen 18080051).

Genes were quantified by real-time PCR using SYBR Green primers (Life Technologies) and was conducted on Applied Biosystems Step One Plus. Data analysis was carried out using log 2-fold change normalized to glyceraldehyde-3-phosphate dehydrogenase (GAPDH) gene expression.

Western Blot

Tissues were lysed in commercial RIPA buffer (Alfa Aesar J63306), with protease inhibitor (Millipore-Sigma P8340) and Triton-X-100 (Fisher BioReagents BP151) added. Samples were incubated with a reducing agent (Invitrogen NP0009) and buffer (Invitrogen B0007) at room temperature for 20 minutes and loaded into either 4-20% or 10% polyacrylamide gels (Bio-Rad #4561094) and transferred onto a PVDF membrane (Immobilon-P IPVH00005).

Membranes stained for Nav1.5 were blocked overnight at 4°C with 5% milk powder in tris-buffered saline (TBS), and then stained overnight at 4°C using the Nav1.5 primary antibody at a 1:100 dilution in 5%

milk powder in TBS with 0.2% Tween-20 (TBS-T). Secondary antibody staining occurred at room temperature for 1 hour in 5% milk powder/TBS-T. Washing steps occurred at room temperature in 5% milk powder/TBS-T.

Membranes stained for Cx43 and GAPDH were blocked for 1 hour at room temperature in 5% bovine serum albumin in TBS. Primary and secondary antibody staining occurred for 1 hour at room temperature, with the antibodies diluted in TBS-T.

The SuperSignal West Dura substrate was used for detection (Thermo Scientific 34076) on a Syngene PXi, with ImageJ used to analyze the data.

Optical analysis of action potential waveforms and calcium transients

These cells were genetically modified to express GCaMP6f to image calcium handling dynamics, and Berst-1 voltage sensitive dye [41] was used to visualize the action potential. Tissues were imaged on a Nikon Eclipse Tsr2 inverted microscope equipped with a Hamamatsu ORCA Flash 4.0 V3 digital CMOS camera and a Lumencor AURA light engine. A Tokai thermal plate was used to maintain µHM temperature during imaging. Videos were imaged at 200-450 fps. The MATLAB Bio-Formats package was used along with custom MATLAB software to calculate waveform parameters. To calculate conduction velocity, we use a modified version of the open-source MATLAB software Rhythm 1.0 [42].

Pharmacology Study

Saxitoxin (SRM NIST, Product # 8642a) was received in a solution of 80% acidified water (pH 3.5)/20% ethanol. Nifedipine (Sigma-Aldrich, Product #N7634) was initially dissolved in dimethyl sulfoxide. E4031 (Alomone Lab, Cat. #E-500) was initially dissolved in MilliQ water. The maximum percentage of DMSO in the total media for tissues treated with nifedipine was 0.02% at 2 µM of drug, which was considered negligible. All pharmaceuticals were dissolved into clear RPMI1640/B27 at 10x the desired final concentration, and added to tissues by changing 10% of the media to limit shock due to full media changes. Tissues were allowed to equilibrate for 15 minutes at 37°C before imaging.

µHM Field Pacing

Fridericia's formula was used to beat-rate correct waveform parameters. To ensure Fridericia's formula was relevant for comparing action potential and calcium handling dynamics across variable beat rates for

different tissues, field pacing was used for certain tissues at day 15. 1-3 Hz field pacing was applied using a Myo-pacer EP instrument (IonOptics). Two electrodes were positioned into the wells so that the applied voltage traveled through the individual tissues. 30V, 20 ms bipolar pulse trains were applied. This formula was found to accurately convert the measurements up to 3Hz, which was deemed appropriate for our data as no tissues spontaneously beat above approximately 3Hz (Fig. S3B).

Statistical Analysis

GraphPad Prism 8.3.1 was used for statistical analysis. Ordinary one-way ANOVA was used for comparing multiple data groups before performing post-hoc Holm-Sidak mean comparison test. *P* value < 0.05 was considered statistically significant difference. * = $p < 0.05$; ** = $p < 0.005$; *** = $p < 0.0005$. Non-linear curve fitting and determination of EC_{50} were performed using a 3-parameter fit.

Acknowledgements

This work was supported by the Department of Biomedical Engineering at Washington University in St. Louis, the American Heart Association (19CDA34730016 to NH, predoctoral fellowship 828938 to JG), the National Institutes of Health (NHLBI R01HL159094 to NH), and the Center for Engineering MechanoBiology, an NSF Science & Technology Center (CMMI: 15-48571 to DWS, GR).

We thank Dr. Michael Vahey for use of his confocal microscope, Dr. Guy Genin for advice on finite element modeling, Dr. Jon Silva for his advice on pharmacologic inhibition of action potential ion channels, Drs. Stacey Rentschler and Jeanne Nerbonne for advice on Western analysis of sodium channels and Cx43 along with positive control lysates from adult mouse ventricular tissues, and members of the Dr. Elizabeth Haswell lab for help with western blot imaging.

Author contributions

D.W.S. and N.H. designed experiments and wrote the manuscript. D.R.S., D.W.S., and N.H. carried out data analysis and interpretation. D.W.S., D.R.S., J.G., K.O., G.R., M.K.M., B.K., and M.P. performed experiments. N.H. supervised and funded the research. All authors were involved in manuscript revisions.

References

[1] F. Stillitano *et al.*, “Modeling susceptibility to drug-induced long QT with a panel of subject-specific induced pluripotent stem cells,” *Elife*, vol. 6, pp. 1–24, 2017, doi: 10.7554/eLife.19406.

[2] K. Musunuru *et al.*, *Induced Pluripotent Stem Cells for Cardiovascular Disease Modeling and Precision Medicine: A Scientific Statement From the American Heart Association*, vol. 11, no. 1. 2018. doi: 10.1161/HCG.0000000000000043.

[3] T. Boudou *et al.*, “A microfabricated platform to measure and manipulate the mechanics of engineered cardiac microtissues,” *ASME 2012 Summer Bioengineering Conference, SBC 2012*, pp. 243–244, 2012, doi: 10.1115/SBC2012-80204.

[4] N. Huebsch *et al.*, “Miniaturized iPS-Cell-Derived Cardiac Muscles for Physiologically Relevant Drug Response Analyses,” *Scientific Reports*, vol. 6, no. 1, p. 24726, Jul. 2016, doi: 10.1038/srep24726.

[5] I. Y. Shadrin *et al.*, “Cardiopatch platform enables maturation and scale-up of human pluripotent stem cell-derived engineered heart tissues,” *Nature Communications*, vol. 8, no. 1, 2017, doi: 10.1038/s41467-017-01946-x.

[6] K. Ronaldson-Bouchard *et al.*, “Advanced maturation of human cardiac tissue grown from pluripotent stem cells,” *Nature*, vol. 556, no. 7700, pp. 239–243, 2018, doi: 10.1038/s41586-018-0016-3.

[7] J. Guo *et al.*, “Elastomer-grafted iPSC-derived micro heart muscles to investigate effects of mechanical loading on physiology,” *ACS Biomaterials Science and Engineering*, vol. 7, no. 7, pp. 2973–2989, 2021, doi: 10.1021/acsbiomaterials.0c00318.

[8] O. J. Abilez *et al.*, “Passive Stretch Induces Structural and Functional Maturation of Engineered Heart Muscle as Predicted by Computational Modeling,” *Stem Cells*, vol. 36, no. 2, pp. 265–277, 2018, doi: 10.1002/stem.2732.

[9] H. J. Auman, H. Coleman, H. E. Riley, F. Olale, H. J. Tsai, and D. Yelon, “Functional modulation of cardiac form through regionally confined cell shape changes,” *PLoS Biology*, vol. 5, no. 3, pp. 0604–0615, 2007, doi: 10.1371/journal.pbio.0050053.

[10] M. Gewillig *et al.*, “Premature foetal closure of the arterial duct: Clinical presentations and outcome,” *European Heart Journal*, vol. 30, no. 12, pp. 1530–1536, 2009, doi: 10.1093/eurheartj/ehp128.

[11] T. W. Wu, T. Azhibekov, and I. Seri, “Transitional hemodynamics in preterm neonates: Clinical relevance,” *Pediatrics and Neonatology*, vol. 57, no. 1, pp. 7–18, 2016, doi: 10.1016/j.pedneo.2015.07.002.

[12] C. H. Lin, G. Bin Lee, B. W. Chang, and G. L. Chang, “A new fabrication process for ultra-thick microfluidic microstructures utilizing SU-8 photoresist,” *Journal of Micromechanics and Microengineering*, vol. 12, no. 5, pp. 590–597, 2002, doi: 10.1088/0960-1317/12/5/312.

[13] M. A. Smith *et al.*, “Design, simulation, and fabrication of three-dimensional microsystem components using grayscale photolithography,” *Journal of Micro/Nanolithography, MEMS, and MOEMS*, vol. 18, no. 04, p. 1, 2019, doi: 10.1117/1.jmm.18.4.043507.

[14] A. Taguchi, A. Nakayama, R. Oketani, S. Kawata, and K. Fujita, “Multiphoton-Excited Deep-Ultraviolet Photolithography for 3D Nanofabrication,” *ACS Applied Nano Materials*, vol. 3, no. 11, pp. 11434–11441, 2020, doi: 10.1021/acsanm.0c02519.

[15] G. Comina, A. Suska, and D. Filippini, “PDMS lab-on-a-chip fabrication using 3D printed templates,” *Lab on a Chip*, vol. 14, no. 2, pp. 424–430, 2014, doi: 10.1039/c3lc50956g.

[16] H. N. Chan, Y. Chen, Y. Shu, Y. Chen, Q. Tian, and H. Wu, “Direct, one-step molding of 3D-printed structures for convenient fabrication of truly 3D PDMS microfluidic chips,” *Microfluidics and Nanofluidics*, vol. 19, no. 1, pp. 9–18, 2015, doi: 10.1007/s10404-014-1542-4.

[17] C. C. Glick *et al.*, “Rapid assembly of multilayer microfluidic structures via 3D-printed transfer molding and bonding,” *Microsystems and Nanoengineering*, vol. 2, no. April, pp. 1–9, 2016, doi: 10.1038/micronano.2016.63.

[18] M. E. Afshar *et al.*, “A 96-well culture platform enables longitudinal analyses of engineered human skeletal muscle microtissue strength,” *Scientific Reports*, vol. 10, no. 1, pp. 1–16, 2020, doi: 10.1038/s41598-020-62837-8.

[19] C. Chande *et al.*, “Universal method for fabricating PDMS microfluidic device using SU8, 3D printing and soft lithography,” *Technology (Singap World Sci)*, vol. 08, no. 01n02, pp. 50–57, 2020, doi: 10.1142/s2339547820500041.

[20] A. Iuliano *et al.*, “Coupling 3D Printing and Novel Replica Molding for In House Fabrication of Skeletal Muscle Tissue Engineering Devices,” *Advanced Materials Technologies*, vol. 5, no. 9, pp. 1–9, 2020, doi: 10.1002/admt.202000344.

[21] A. O. Olanrewaju, A. Robillard, M. Dagher, and D. Juncker, “Autonomous microfluidic capillaric circuits replicated from 3D-printed molds,” *Lab on a Chip*, vol. 16, no. 19, pp. 3804–3814, 2016, doi: 10.1039/c6lc00764c.

[22] H. N. Chan, Y. Shu, Q. Tian, Y. Chen, Y. Chen, and H. Wu, “Replicating 3D printed structures into hydrogels,” *Materials Horizons*, vol. 3, no. 4, pp. 309–313, 2016, doi: 10.1039/c6mh00058d.

[23] C. M. Olmos *et al.*, “Epoxy resin mold and PDMS microfluidic devices through photopolymer flexographic printing plate,” *Sensors and Actuators, B: Chemical*, vol. 288, no. March, pp. 742–748, 2019, doi: 10.1016/j.snb.2019.03.062.

[24] K. S. Anseth, C. N. Bowman, and L. Brannon-Peppas, “Mechanical properties of hydrogels and their experimental determination,” *Biomaterials*, vol. 17, no. 17, pp. 1647–1657, 1996, doi: 10.1016/0142-9612(96)87644-7.

[25] W. R. Legant, A. Pathak, M. T. Yang, V. S. Deshpande, R. M. McMeeking, and C. S. Chen, “Microfabricated tissue gauges to measure and manipulate forces from 3D microtissues,” *Proc Natl Acad Sci U S A*, vol. 106, no. 25, pp. 10097–10102, 2009, doi: 10.1073/pnas.0900174106.

[26] X. Lian *et al.*, “Robust cardiomyocyte differentiation from human pluripotent stem cells via temporal modulation of canonical Wnt signaling,” *Proc Natl Acad Sci U S A*, vol. 109, no. 27, pp. 1–10, 2012, doi: 10.1073/pnas.1200250109.

[27] P. Bose, J. Eyckmans, T. D. Nguyen, C. S. Chen, and D. H. Reich, “Effects of Geometry on the Mechanics and Alignment of Three-Dimensional Engineered Microtissues,” *ACS Biomaterials Science and Engineering*, vol. 5, no. 8, pp. 3843–3855, 2019, doi: 10.1021/acsbiomaterials.8b01183.

[28] N. Huebsch *et al.*, “Metabolically driven maturation of human-induced-pluripotent-stem-cell-derived cardiac microtissues on microfluidic chips,” *Nature Biomedical Engineering*, vol. 6, no. 4, pp. 372–388, Apr. 2022, doi: 10.1038/s41551-022-00884-4.

[29] G. Li *et al.*, “Differential Wnt-mediated programming and arrhythmogenesis in right versus left ventricles,” *Journal of Molecular and Cellular Cardiology*, vol. 123, no. April, pp. 92–107, 2018, doi: 10.1016/j.yjmcc.2018.09.002.

[30] T. Grancharova *et al.*, “A comprehensive analysis of gene expression changes in a high replicate and open-source dataset of differentiating hiPSC-derived cardiomyocytes,” *Scientific Reports*, vol. 11, no. 1, pp. 1–21, 2021, doi: 10.1038/s41598-021-94732-1.

[31] J. M. Rhett, E. L. Ongstad, J. Jourdan, and R. G. Gourdie, “Cx43 associates with Nav1.5 in the cardiomyocyte perinexus,” *Journal of Membrane Biology*, vol. 245, no. 7, pp. 411–422, 2012, doi: 10.1007/s00232-012-9465-z.

[32] R. M. Shaw, A. J. Fay, M. A. Puthenveedu, M. von Zastrow, Y. N. Jan, and L. Y. Jan, “Microtubule Plus-End-Tracking Proteins Target Gap Junctions Directly from the Cell Interior to Adherens Junctions,” *Cell*, vol. 128, no. 3, pp. 547–560, 2007, doi: 10.1016/j.cell.2006.12.037.

[33] A. J. Shanker, K. Yamada, K. G. Green, K. A. Yamada, and J. E. Saffitz, “Matrix protein-specific regulation of Cx43 expression in cardiac myocytes subjected to mechanical load,” *Circulation Research*, vol. 96, no. 5, pp. 558–566, 2005, doi: 10.1161/01.RES.0000158964.42008.a2.

[34] S. Sengupta, K. E. Rothenberg, H. Li, B. D. Hoffman, and N. Bursac, “Altering integrin engagement regulates membrane localization of Kir2.1 channels,” *J Cell Sci*, vol. 132, no. 17, 2019, doi: 10.1242/jcs.225383.

[35] G. A. Marchal *et al.*, “Targeting the Microtubule EB1-CLASP2 Complex Modulates NaV1.5 at Intercalated Discs,” *Circulation Research*, pp. 349–365, 2021, doi: 10.1161/CIRCRESAHA.120.318643.

[36] K. Yamada, K. G. Green, A. M. Samarel, and J. E. Saffitz, “Distinct pathways regulate expression of cardiac electrical and mechanical junction proteins in response to stretch,” *Circulation Research*, vol. 97, no. 4, pp. 346–353, 2005, doi: 10.1161/01.RES.0000178788.76568.8a.

[37] X. Zhao, N. Huebsch, D. J. Mooney, and Z. Suo, “Stress-relaxation behavior in gels with ionic and covalent crosslinks,” *Journal of Applied Physics*, vol. 107, no. 6, 2010, doi: 10.1063/1.3343265.

[38] H. J. Kong, K. Y. Lee, and D. J. Mooney, “Decoupling the dependence of rheological/mechanical properties of hydrogels from solids concentration,” *Polymer (Guildf)*, vol. 43, no. 23, pp. 6239–6246, 2002, doi: 10.1016/S0032-3861(02)00559-1.

[39] J. Zhu and R. E. Marchant, “Design properties of hydrogel tissue-engineering scaffolds,” *Expert Review of Medical Devices*, vol. 8, no. 5, pp. 607–626, 2011, doi: 10.1586/erd.11.27.

[40] R. Jumaidin, S. M. Sapuan, M. Jawaid, M. R. Ishak, and J. Sahari, “Effect of agar on physical properties of thermoplastic starch derived from sugar palm tree,” *Pertanika Journal of Science and Technology*, vol. 25, no. 4, pp. 1235–1248, 2017.

[41] Y. L. Huang, A. S. Walker, and E. W. Miller, “A Photostable Silicon Rhodamine Platform for Optical Voltage Sensing,” *J Am Chem Soc*, vol. 137, no. 33, pp. 10767–10776, 2015, doi: 10.1021/jacs.5b06644.

[42] J. I. Laughner, F. S. Ng, M. S. Sulkin, R. Martin Arthur, and I. R. Efimov, “Processing and analysis of cardiac optical mapping data obtained with potentiometric dyes,” *American Journal of Physiology - Heart and Circulatory Physiology*, vol. 303, no. 7, 2012, doi: 10.1152/ajpheart.00404.2012.

Figure Captions

Figure 1. Hydrogel intermediates enable replication of high-resolution 3D-prints into elastomer.

A: CAD model of 3D-print and brightfield images of PDMS molded directly off of stereolithographic 3D-print or SU-8.

B: Schematic describing hypothesized mechanism of PDMS free-radical crosslinking inhibition at interface with high-resolution stereolithographic 3D-print.

C: Schematic describing Hydrogel Assisted Stereolithographic Elastomer methodology to replicate 3D-prints into PDMS. The hydrogel (agar or alginate) is allowed to crosslink around the 3D-print, creating a negative replica of the desired features. The PDMS elastomer is then crosslinked around the hydrogel negative, resulting in PDMS replication of the original 3D-print.

D: Pure covalently crosslinked alginate was completely incapable of replication due to its brittle nature. Representative images of agar and alginate broadly replicating 3D-printed features into PDMS with varying degrees of success.

E: Quantification of hydrogel properties most correlated with replication fidelity. 3D-printed dogbone stencils were molded using a variety of agar and alginate concentrations, with the resulting PDMS dogbone compared to the original shape (human assigned scoring on a scale of 1-5). Error bars: SD

F-H: Representative CAD and scanning electron microscope images of 3D-printed shapes replicated in PDMS via HASTE method that would be difficult or impossible to create using standard photolithography methods.

Figure 2. Prestress regulates cell morphology in Micro-Heart Muscle (µHM).

A) Timeline of iPSC small molecule-based differentiation to cardiomyocytes, the subsequent seeding into the µHM format, and the measurements of cell morphology, electrophysiology, and pharmacology experiments at the terminal time point.

B) COMSOL modeling images depicting increased tissue preload with increased shaft length.

C) Representative bright field images taken at µHM day 15 (µD15) showing grossly similar tissue morphology regardless of tissue size.

D) Quantification of µHM shaft lateral compaction at µD15 ($n > 150$ µHM) (*: $p < 0.05$, **: $p < 0.005$, ***: $p < 0.0005$, error bars: SEM).

E) Representative confocal images of nuclei (Hoechst/blue) and sarcomeric α–actinin (green) of 0mm and 2mm tissues at µD15.

F) Quantification of the effects of tissue geometry on nuclear alignment and nuclear aspect ratio at µD15 ($n > 12$ µHM) (*: $p < 0.05$, **: $p < 0.005$, ***: $p < 0.0005$, error bars: SEM).

G) Representative confocal images of nuclei (Hoechst/blue) and cell membrane (wheat germ agglutinin/green) of 0mm and 2mm tissues at µD15.

H) Quantification of the effects of tissue geometry on cell length and width at µD15. ($n >100$ cells, *: $p < 0.05$, **: $p < 0.005$, ***: $p < 0.0005$, error bars: SEM)

Figure 3: Tissue prestress regulates µHM Electrophysiology.

A) Representative action potential and calcium handling waveforms for 0mm, 1mm, and 2mm µHM at µD15.

B) Electrophysiology heatmap of action potential and calcium handling dynamics for µHM of shaft length 0, 1, & 2mm long. Data represented as fold change, normalized to µD5 0mm data for given parameter.

C) Quantification of spontaneous beat rate, beat-rate corrected action potential upstroke duration, and spontaneous conduction velocity for 0, 1, & 2mm µHM up to µD15 ($n > 100$ µHM, *: $p < 0.05$, **: $p < 0.005$, ***: $p < 0.0005$, error bars: SEM).

D) Representative conduction velocity maps for 1 & 2mm µHM at µD15.

E-G) Response of µHM to pharmacologic inhibition of ion channels: effect of E) STX on upstroke duration, F) nifedipine on calcium transient amplitude, and G) E4031 on APD_{90} (n = 20-30 µHM). Error bars: SEM

Figure 4: Changes in Sodium Channels and Gap-junctions Are Regulated in a Post-Translational Manner

A) Relative expression of 12 genes encoding for mechanical and action potential-related ion channels in µHM at µD15: ACTN2, PKP2, JUP1, MYH7, MYL2, SCN5A, CACNA1C, KCNH1, KCNJ12, RYR2, ATP2A2, and GJA1. Error bars: SEM

B) Representative staining of 0mm and elongated µHM at µD15 for: Plakophilin-2, Nav.15, and Connexin-43

C) Representative Western blot of 0mm and elongated µHM at µD15 for: Nav1.5, Connexin-43, and GAPDH

Figure 1

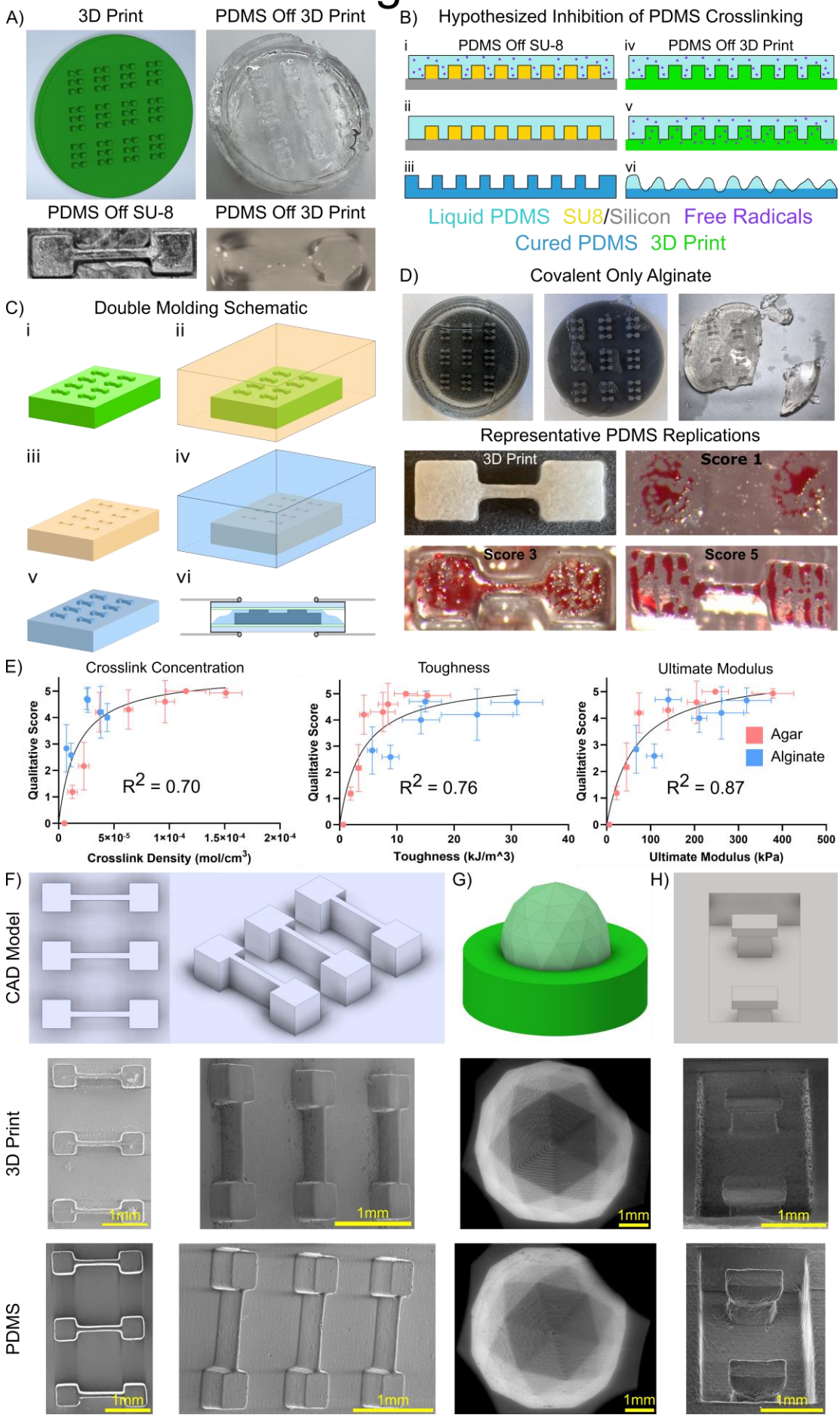
A)
3D Print
PDMS Off 3D Print
PDMS Off SU-8
PDMS Off 3D Print
B) Hypothesized Inhibition of PDMS Crosslinking
i PDMS Off SU-8
iv PDMS Off 3D Print
ii
v
iii
vi
Liquid PDMS SU8/Silicon Free Radicals
Cured PDMS 3D Print
C) Double Molding Schematic
i
ii
iii
iv
v
vi
D) Covalent Only Alginate
Representative PDMS Replications
3D Print
Score 1
Score 3
Score 5
E)
Crosslink Concentration
Toughness
Ultimate Modulus
Qualitative Score
R2 = 0.70
R2 = 0.76
R2 = 0.87
Agar
Alginate
Crosslink Density (mol/cm3)
Toughness (kJ/m^3)
Ultimate Modulus (kPa)
F)
G)
H)
CAD Model
3D Print
PDMS
1mm

Figure 2

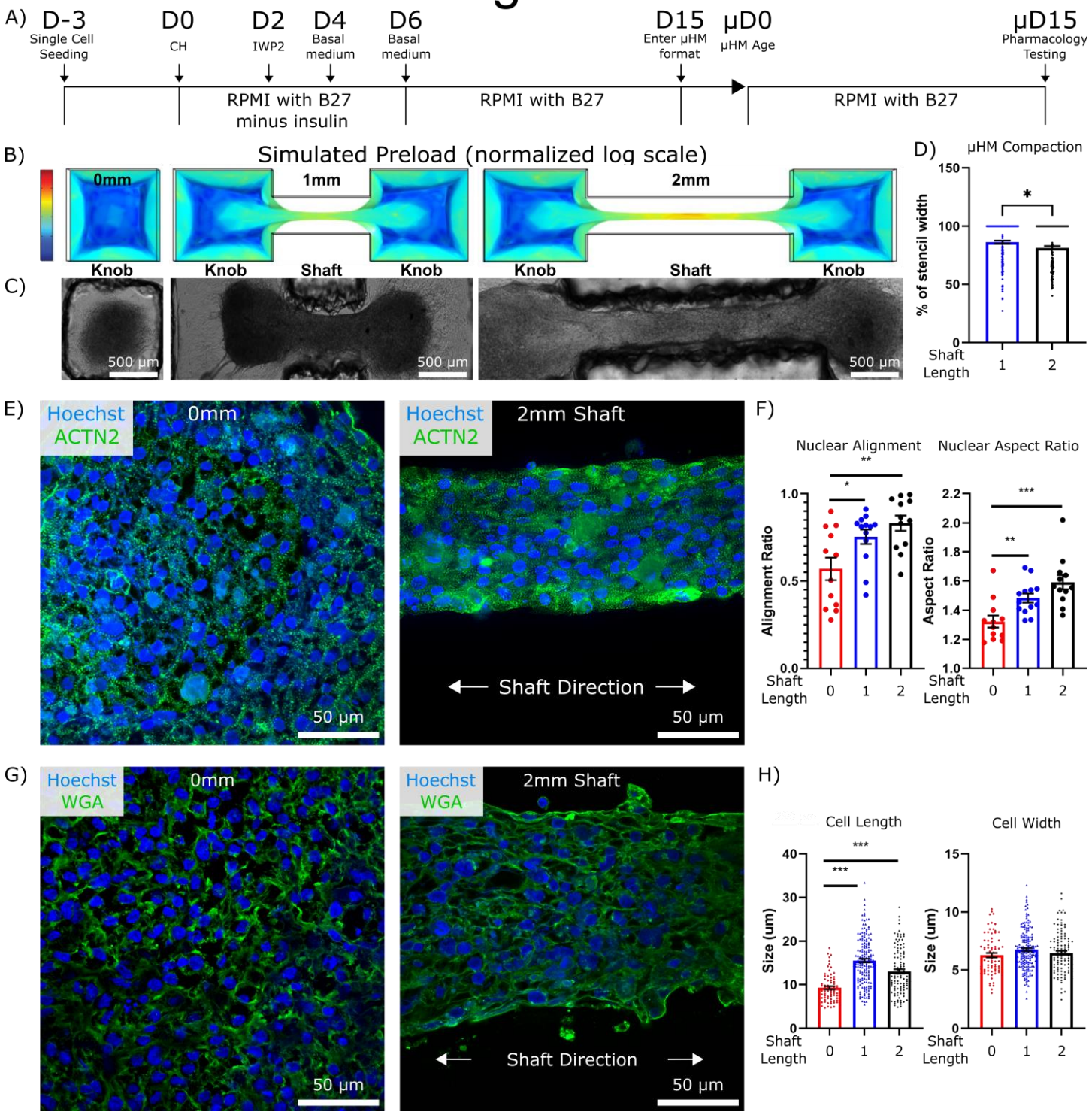
A)
D-3
Single Cell Seeding
D0
CH
D2
IWP2
D4
Basal medium
D6
Basal medium
D15
Enter μHM format
μD0
μHM Age
μD15
Pharmacology Testing
RPMI with B27 minus insulin
RPMI with B27
RPMI with B27
B)
Simulated Preload (normalized log scale)
0mm
1mm
2mm
Knob
Knob
Shaft
Knob
Knob
Shaft
Knob
C)
500 μm
500 μm
500 μm
D)
μHM Compaction
% of stencil width
Shaft Length
E)
Hoechst
ACTN2
0mm
50 μm
Hoechst
ACTN2
2mm Shaft
Shaft Direction
50 μm
F)
Nuclear Alignment
Nuclear Aspect Ratio
Alignment Ratio
Aspect Ratio
Shaft Length
G)
Hoechst
WGA
0mm
50 μm
Hoechst
WGA
2mm Shaft
Shaft Direction
50 μm
H)
Cell Length
Cell Width
Size (um)
Shaft Length

Figure 3

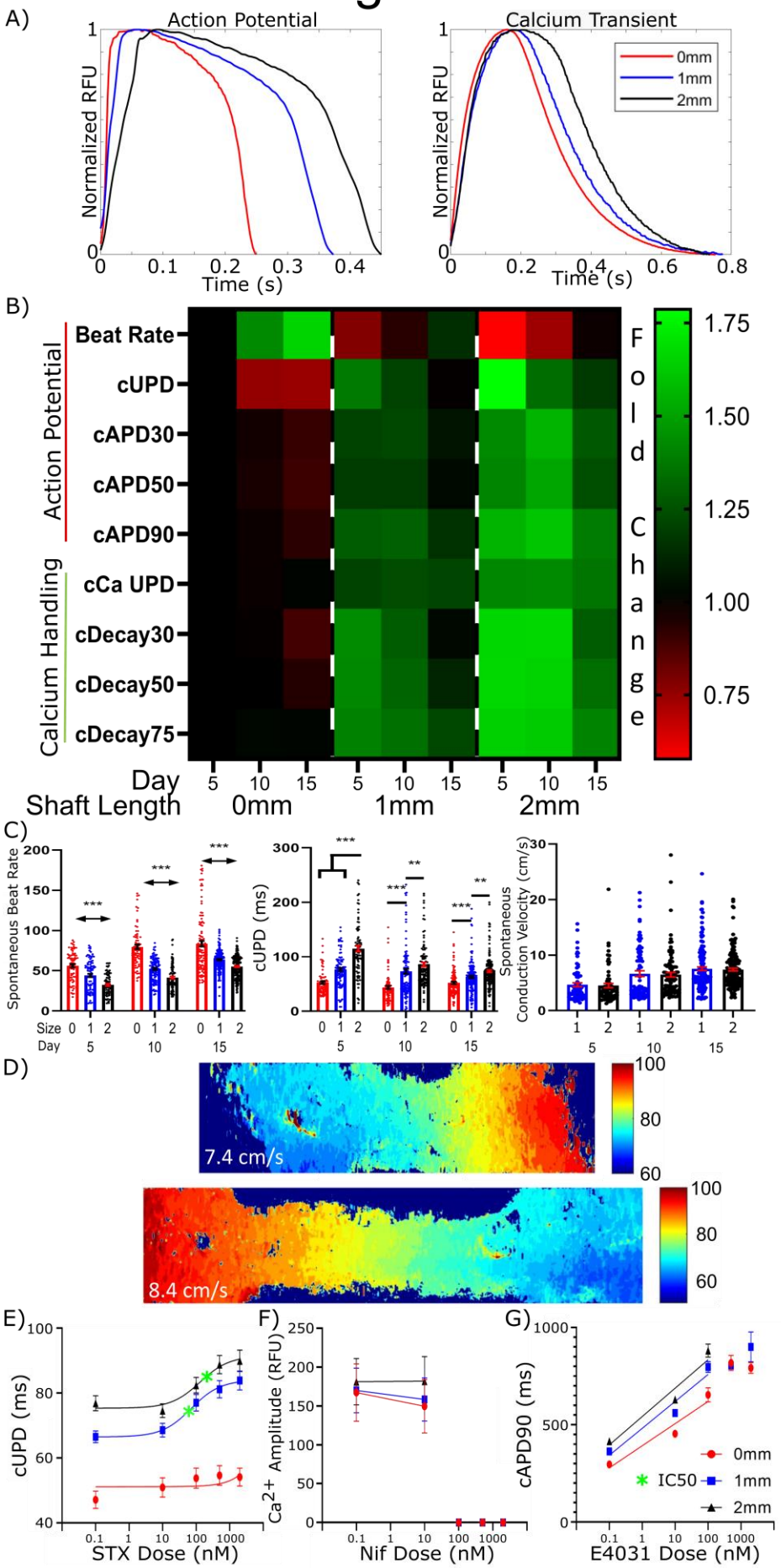
A)
Action Potential
Calcium Transient
Normalized RFU
Time (s)
0mm
1mm
2mm
B)
Action Potential
Calcium Handling
Beat Rate
cUPD
cAPD30
cAPD50
cAPD90
cCa UPD
cDecay30
cDecay50
cDecay75
Fold Change
Day
Shaft Length
0mm
1mm
2mm
C)
Spontaneous Beat Rate
cUPD (ms)
Spontaneous Conduction Velocity (cm/s)
Size
Day
D)
7.4 cm/s
8.4 cm/s
E)
cUPD (ms)
STX Dose (nM)
F)
Ca2+ Amplitude (RFU)
Nif Dose (nM)
G)
cAPD90 (ms)
E4031 Dose (nM)
IC50

Figure 4

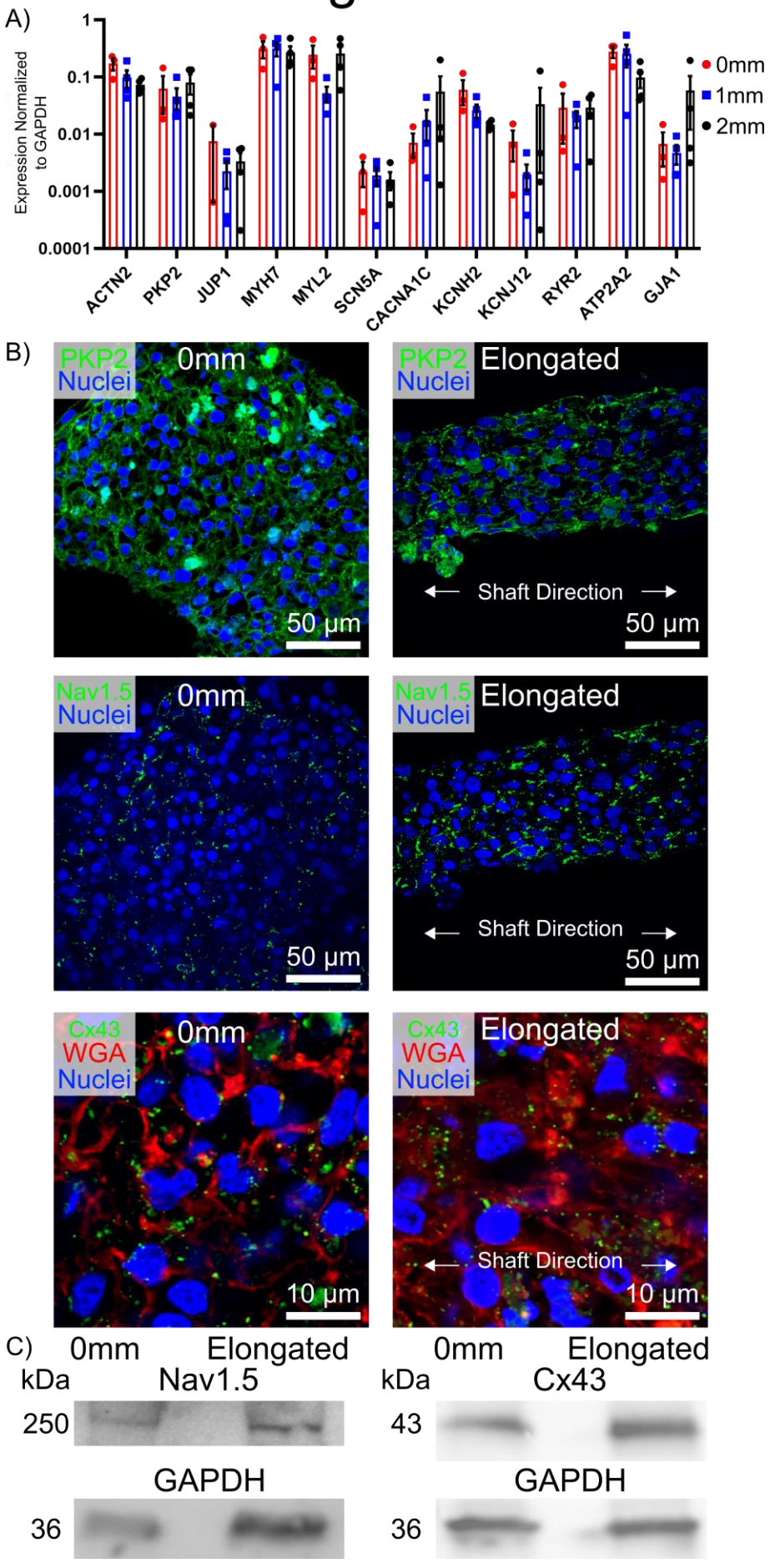
A)
Expression Normalized to GAPDH
1
0.1
0.01
0.001
0.0001
0mm
1mm
2mm
ACTN2
PKP2
JUP1
MYH7
MYL2
SCN5A
CACNA1C
KCNH2
KCNJ12
RYR2
ATP2A2
GJA1
B)
PKP2
Nuclei
0mm
50 µm
PKP2
Nuclei
Elongated
Shaft Direction
50 µm
Nav1.5
Nuclei
0mm
50 µm
Nav1.5
Nuclei
Elongated
Shaft Direction
50 µm
Cx43
WGA
Nuclei
0mm
10 µm
Cx43
WGA
Nuclei
Elongated
Shaft Direction
10 µm
C)
0mm
Elongated
kDa
Nav1.5
250
GAPDH
36
0mm
Elongated
kDa
Cx43
43
GAPDH
36